Dzyaloshinskii-Moriya interaction and chiral damping effect in symmetric epitaxial Pd/Co/Pd(111) trilayers

A. V. Davydenko [1,*] A. G. Kozlov [1] M. E. Stebliy,[1] A. G. Kolesnikov,[1] N. I. Sarnavskiy [1]
I. G. Iliushin [2] and A. P. Golikov [3]

[1]*Laboratory of Thin Film Technologies, School of Natural Sciences, Far Eastern Federal University, Vladivostok, 690950, Russia*
[2]*Department of Theoretical and Nuclear Physics, School of Natural Sciences, Far Eastern Federal University, Vladivostok, 690950, Russia*
[3]*Institute of Chemistry FEB RAS, Vladivostok, 690022, Russia*

We investigate the creep of domain walls (DWs) in the combination of in-plane (IP) and out-of-plane magnetic fields in a series of epitaxial Cu(2 nm)/Pd(0–3 nm)/Co(0.7 nm)/Pd(3 nm) samples. Measured velocity curves, $v(H_x)$, are fitted with an extended dispersive elasticity model, which considers the dependence of both the elastic energy of the DWs and a velocity prefactor in the creep law on the IP magnetic field. The results of the calculations indicate that strong asymmetry in the $v(H_x)$ curves in the investigated system is primarily defined by the dependence of the velocity prefactor on the IP magnetic field, which may be related to a chiral damping effect. The effective energy of the Dzyaloshinskii-Moriya interaction (DMI) increases with increasing thickness of the Pd bottom layer from -0.16 ± 0.03 to $0.19 \pm 0.05 \, \mathrm{mJ/m^2}$. We attribute the complex dependence of the effective DMI energy on the thickness of the Pd bottom layer in the epitaxial Pd/Co/Pd(111) system and the existence of the nonzero DMI in the symmetric Pd(3 nm)/Co(0.7 nm)/Pd(3 nm) samples to unequal strains in the bottom Pd/Co and top Co/Pd interfaces. The elastic strains in the interfaces varying depending on the thickness of the Pd bottom layer strongly influence the magnitude and even the sign of the contributions to the net DMI energy from each interface.

I. INTRODUCTION

The Dzyaloshinskii-Moriya interaction (DMI) is an intriguing phenomenon that has recently attracted significant interest due to the possibility of using it in racetrack memory devices [1,2]. The DMI has a predominate contribution from the interfaces in multilayered heavy metal-ferromagnetic (FM) structures because the inversion symmetry is broken in the interface layers [3]. This type of DMI in multilayered structures or superlattices is referred to as an interfacial DMI. The interfacial DMI may stabilize chiral Néel domain walls (DWs) [4]. Chiral Néel DWs are effectively displaced by the current pulses due to a spin-orbit torque effect with the direction of the DW propagation relative to the current direction depending on the sign of the DMI [5]. Chiral Néel DWs reach larger velocities under the influence of the current pulses than achiral Bloch DWs [6,7].

The net interfacial DMI in symmetric multilayered systems should be absent because the effective contributions to the DMI from the bottom and top interfaces should compensate each other. Experimental data for the most investigated symmetric systems with perpendicular magnetic anisotropy (PMA), Pt/FM/Pt and Pd/FM/Pd, indicate that the weak DMI in symmetric systems is a more common phenomenon [8–12]. The nonzero DMI in symmetric systems is often explained by different properties of bottom and top interfaces, such as strains [13], structural quality [14], roughness, and sharpness

[11]. Rather strong DMIs were reported in some symmetric systems: $-0.8 \, \mathrm{mJ/m^2}$ in Pt(5 nm)/Co(0.7 nm)/Pt(5 nm) [14]; $-1.3 \, \mathrm{mJ/m^2}$ in Pt(4 nm)/Co(0.7 nm)/Pt(2 nm) [13]. It is noteworthy that the large DMI values in the systems were measured by the asymmetry of DW propagation in a creep regime under the influence of out-of-plane (OOP) and in-plane (IP) magnetic fields by the method originally introduced by Je *et al.* [8]. They found that the velocity curves $v(H_x)$ of the DWs that are perpendicular to the IP magnetic field are symmetric relative to the DMI field and demonstrate a minimum if the applied magnetic field compensates the DMI effective field. However, both Brillouin light scattering investigations [9] and spin-orbit torque efficiency measurements [15] did not indicate any sizable DMI in the symmetric Pt/Co/Pt system. In this case, the study of Jué *et al.* [16] deserves special attention. The authors explained $v(H_x)$ asymmetry in Pt/Co/Pt trilayers not by the DMI, but by a chiral damping that influenced the DW mobility. This asymmetric chiral contribution was considered in some of the latest studies concerning DW propagation in a combination of OOP and IP magnetic fields [17,18].

In this paper, we investigate the symmetric epitaxial Pd/Co/Pd(111) system and provide insights into the reason for the strongly asymmetric $v(H_x)$ curves found in this system previously [19]. We consider a series of Pd/Co/Pd samples with a constant Co thickness of 0.7 nm and a variable Pd bottom layer thickness. Experimental data are fitted by the extended dispersive stiffness theoretical model. The obtained results are discussed and compared with similar results measured in various systems.

*avdavydenko@gmail.com

II. EXTENDED DISPERSIVE STIFFNESS MODEL

Consider a general creep law for DWs in the form postulated by Jeudy *et al.* in Ref. [20]:

$$v(H_z, H_x, T) = v_0(H_x, T) \exp\left(-\frac{\Delta E}{k_B T}\right), \qquad (1)$$

where $v(H_z, H_x, T)$ is a velocity of the DW, $v_0(H_x, T)$ is a characteristic velocity of the DW at $H_z = H_d$, H_d is a depinning field, T is the absolute temperature, k_B is the Boltzmann constant, and

$$\Delta E = k_B T_d \left[\left(\frac{H_z}{H_d}\right)^{-1/4} - 1\right], \qquad (2)$$

is an energy barrier with $k_B T_d$ equal to a characteristic pinning energy scale.

Considering low velocities under the driving field much less than the depinning field, $H_z \ll H_d$, the unit in Eq. (2) may be neglected, and the creep law takes the well-known form

$$
\begin{aligned}
v(H_z, H_x, T) &= v_0(H_x, T) \exp\left[-\frac{T_d}{T}\left(\frac{H_z}{H_d}\right)^{-1/4}\right] \\
&= v_0(H_x, T) \exp[-\zeta(\mu_0 H_z)^{-1/4}], \qquad (3)
\end{aligned}
$$

where $\zeta = \frac{T_d}{T}(\mu_0 H_d)^{1/4}$ responds to the IP magnetic field dependence of the velocity.

In their pioneering study, Je *et al.* [8] estimated ζ in Eq. (3) in the form

$$\zeta(H_x) = \zeta(0)\left[\frac{\sigma(H_x)}{\sigma(H_x = 0)}\right]^{1/4}, \qquad (4)$$

where σ is a DW energy density per unit area and $\zeta(0)$ is a constant that does not depend on H_x [8]. The DW energy density of the DW oriented perpendicular to the IP magnetic field was supposed to be nondispersive. This means that it was uniform along the length of the DW. Pellegren *et al.* [21] introduced the dispersive stiffness model of DWs. In the creep regime, the DWs are not displaced by their entire length but rather by small protrusions at which the pinning energy barrier is overcome. The arc-shaped deformations of the DWs under the influence of the driving OOP magnetic field were considered. In the general case, the DW energy density per unit length depends on the orientation of the DW's segment relative to the IP magnetic field and is nonuniform in the arc-shaped deformed region of the DW. Considering stretching, bending, and orientation of the DW in the deformed region, Pellegren *et al.* [21] calculated the dispersive elasticity of the DWs under the action of OOP and IP magnetic fields and successfully modeled asymmetrical $v(H_x)$ curves, which reproduced the experimental results reasonably well. However, the authors did not find an optimal length of the protrusion and treated it as a free parameter.

Hartmann *et al.* [22] thoroughly described and extended this model. The authors considered triangular-shaped protrusions and optimized their lengths depending on the calculated parameters. They considered exchange energy costs due to the kinks in the connection of the deformed DW with the straight DW segments. Unlike the approach of Pellegren *et al.* [21], who calculated only dispersive stiffness in the creep model but found the proportionality constant $\zeta(0)$ in Eq. (4) by fitting the

experimental data, Hartmann *et al.* [22] calculated the energy barrier ΔE in the general creep law based on the structural and scaling parameters, which must take reasonable values.

In most previous studies, it is considered that the IP magnetic field changes only the energy barrier ΔE. However, the possible dependence of the prefactor v_0 on the H_x is usually neglected [8,14,21–23]. Gorchon *et al.* [24] expressed the prefactor v_0 in the universal creep law in the form of

$$v_0(H_x, T) = \xi_0 f_0 \exp\left(\frac{T_d}{T}\right), \qquad (5)$$

where ξ_0 is a disorder correlation length and f_0 is an attempt frequency. Jué *et al.* [16] supposed the attempt frequency scales with the inverse of the damping $f_0 \sim 1/\chi$, where χ is a damping parameter. The key concept of their study was that damping in some systems may be chiral and may depend on the azimuthal orientation of the magnetization in the DWs. Lau *et al.* [17] assumed the following form of the dependence of the velocity prefactor on the IP magnetic field

$$v_0(H_x, T) = v_0^*[1 + \chi^* \cos(\phi - \alpha)], \qquad (6)$$

where v_0^* is a velocity independent of H_x, χ^* is a chiral damping weight, the absolute value of which cannot be >1, ϕ is an angle between the IP magnetization at the DW and the direction of IP magnetic field, and α is an angle between a DW normal and the direction of IP magnetic field. The dependence of v_0 on the IP magnetic field is included in the functions $\phi(H_x)$ and $\alpha(H_x)$. Despite Lau *et al.* [17] did not explain how the expression for the velocity prefactor had been derived, they obtained the excellent coincidence between the results deduced from the fittings of velocity curves and analysis of Brillouin light spectra.

In this paper, we explain the asymmetrical shape of the $v(H_x)$ dependencies measured in epitaxial Pd/Co/Pd(111) trilayers, both by considering the contributions of the IP magnetic field to the energy barrier and the velocity prefactor in the creep law. The energy barrier ΔE in Eq. (1) was calculated using the approach of Hartmann *et al.* [22]. The approach is described in detail in the Supplemental Material [25]. We also recommend familiarization with their study for deeper understanding [22]. The velocity prefactor $v_0(H_x, T)$ was calculated according to the Lau *et al.* [17] approach by Eq. (6) with $\alpha = 0$ and taking the dependence $\phi(H_x)$ from the calculations of the energy barrier.

III. EXPERIMENT

The samples were evaporated in an Omicron ultrahigh vacuum system, which consisted of a molecular beam epitaxy chamber and an analysis chamber interconnected with each other. We used Si(111) substrates misoriented toward [2,11] by 0.1°. Before loading into the chamber, Si(111) substrates were rinsed in isopropyl and distilled water. The substrates were then heated at 800 K by indirect heating for 12 h. Just before deposition, the substrates were flash-heated by direct current at 1400 K three times for 10 s and slowly cooled down to 300 K. All the metals were evaporated from high temperature effusion cells.

The growth rates of Cu, Co, and Pd were 0.9, 0.28, and 0.26 nm/min, respectively. The deposition rates were
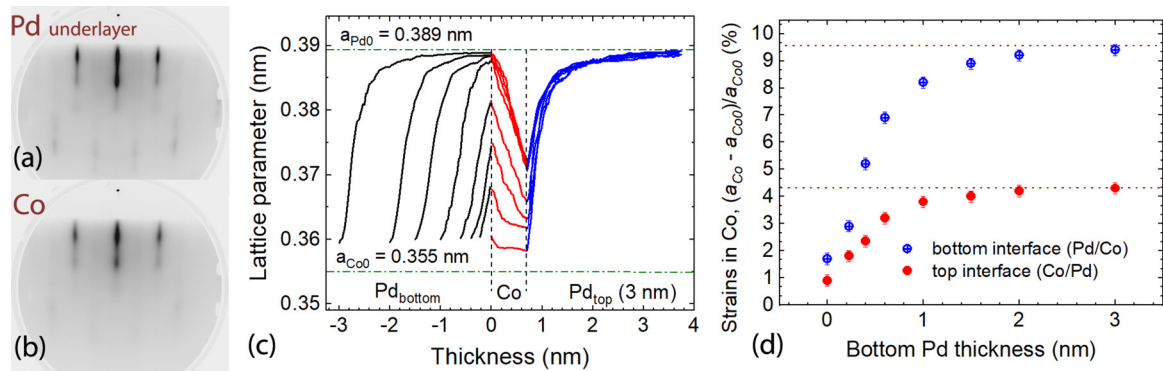
FIG. 1. (a) and (b) Reflection high-energy electron diffraction (RHEED) patterns of Si/Cu(2)/Pd(3) and Si/Cu(2)/Pd(3)/Co(0.7) surfaces, respectively. (c) Lattice parameter measured in the process of the growth of the layers in Pd(d_{Pd})/Co/Pd trilayers. The beginning thicknesses of the growth are shifted to negative values for better comparative analysis of the results. a_{Co0} is a volume lattice parameter of face-centered cubic (fcc) Co. (d) Strains in the bottom Pd/Co and top Co/Pd interfaces.

monitored by a quartz crystal microbalance, which was calibrated by means of reflection high-energy electron diffraction (RHEED). We detected the oscillations of the intensity of the specular beam reflection during the growth of Cu on Si(111), Co on Si(111)/Cu(1 nm), and Pd on Si(111)/Cu(1 nm). We then calculated the period of oscillations and compared it with data obtained from the quartz crystal microbalance. The temperature of the substrates was 340 K during Cu and bottom Pd layer deposition and 370 K during Co and top Pd layers deposition. Changes in the temperature of the samples during the deposition of different materials were caused by different infrared heating of the samples from the effusion cells.

Epitaxial Pd(d_{Pd})/Co(0.7)/Pd(3) trilayers were grown on a Si/Cu(2) surface (hereinafter, all thicknesses are in nanometers). The thickness of the bottom Pd layer d_{Pd} was varied from 0 to 3 nm to investigate the origin of the DMI in this system. In addition, asymmetric Pd(3)/Co(0.7)/Cu(2)/Pd(3) samples were deposited to define from which interface the contribution to the DMI is the largest. The thickness of the Co layer was chosen as 0.7 nm because, for larger Co thicknesses, the anisotropy in the asymmetric Cu/Co/Pd samples was IP. The Pd(d_{Pd})/Co(0.7)/Pd(3) samples will be denoted simply as Pd(d_{Pd}) when it comes to the comparison of symmetric samples only. If the asymmetric Pd/Co/Cu or Cu/Co/Pd samples are compared with the symmetric Pd/Co/Pd samples, we will give the full notation of the samples to avoid misunderstandings. The lattice period of the metal layers during growth and their structure were analyzed by means of RHEED (Staib Instruments). RHEED measurements were carried out simultaneously with deposition of the samples. Magnetic hysteresis loops of the samples were measured using a vibrating sample magnetometer (Lakeshore) with applied magnetic fields of up to 2 T. The magnetic structure was investigated by a magneto-optical Kerr effect (MOKE) microscope (Evico-Magnetics). The MOKE microscope was equipped with a handmade coil applying OOP magnetic fields and an IP electromagnet. The OOP coil was used in pulse mode and produced magnetic fields with an amplitude of up to 50 mT and a width down to 2 ms. The scheme for the measurement of the DW velocity was as follows. A stable nucleating circular domain was found. A constant IP magnetic field was switched on. The pulse of the OOP magnetic field of the calibrated time-length was applied.

The distance at which the DW propagated was measured from a snapshot of differential magnetic contrast made by the Kerr microscope.

IV. RESULTS AND DISCUSSION

A. RHEED investigation

A Cu(2) buffer layer was formed on the Si(111) substrate to prevent intermixing of Pd and Si and to initiate epitaxial growth of face-centered cubic (fcc) Pd(111). The epitaxial relationships defined from the RHEED patterns are Cu(111) ∥ Si(111) and Cu[11-2] ∥ Si[10-1]. The epitaxial relationships during growth of the subsequent Pd and Co layers remain the same as in Cu. Pd(111) grows on Cu(111) and Co(111) surfaces in the fcc structure. Co grows on the Pd(111) surface presumably in the fcc structure [29]. The RHEED patterns from the bottom Pd and Co layers in the Pd(3)/Co(0.7)/Pd(3) sample are shown in Figs. 1(a) and 1(b), respectively. The RHEED streaks confirm the well-ordered crystalline structure of the layers. The evolution of the lattice parameter during the growth of the structures was measured by RHEED [Fig. 1(c)]. There is a large lattice mismatch between Pd and Cu (Co) of 7.9% (9.6%). The bottom Pd layer is initially largely strained when it grows on the Si/Cu(2) surface. Stress is gradually relaxed by the introduction of misfit dislocations in the Pd layers. The bottom Pd layer demonstrates a volume lattice parameter at the thickness of 3 nm.

Co layers grown on the top of Pd underlayers are strained. Strains are partially relaxed during growth of the Co layers. Therefore, strains on the bottom and on the top of the Co layers depend on the thickness of the Pd underlayer [Fig. 1(d)]. Since the thickness of the Co layers was only 0.7 nm, the lattice parameter on the top of the Co layers does not recover to the volume Co lattice parameter.

B. PMA characterization

The OOP and IP magnetic hysteresis loops of the Pd(1)/Co(0.7)/Pd(3) sample are shown in Fig. 2(a). The other samples had similar hysteresis loops. All samples demonstrated PMA. The anisotropy field H_{PMA} changed depending on the Pd bottom layer thickness, as indicated in Fig. 2(b).
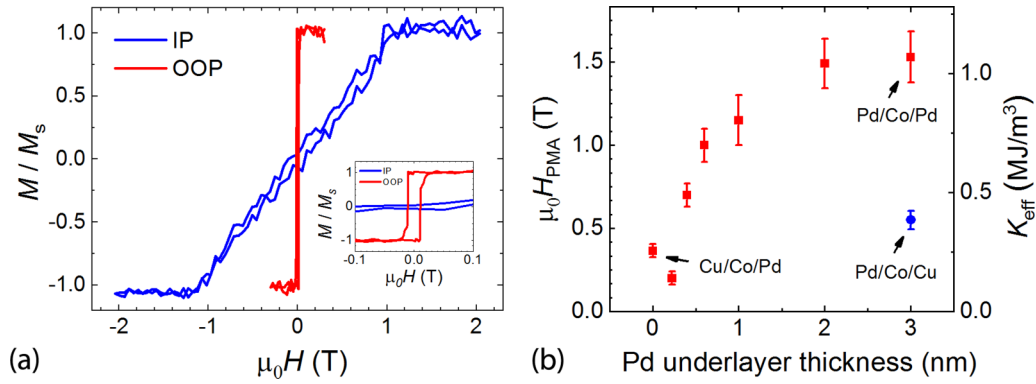
FIG. 2. (a) Out-of-plane (OOP) and in-plane (IP) magnetic hysteresis loops of the Pd(1)/Co(0.7)/Pd(3) sample. (b) Dependencies of the perpendicular magnetic anisotropy (PMA) field and energy of PMA on the thickness of the Pd bottom layer.

In the initial stages of the growth of the Pd bottom layers, the PMA slightly decreased, which may be explained by the partial covering of the Si(111)/Cu surface by Pd atoms and the possible intermixing of Pd with Cu [30]. With further increasing Pd thickness, the PMA increased, which is explained by an increase in a magnetoelastic contribution to the PMA. The general behavior of H_{PMA}, depending on the Pd bottom layer thickness, is correlated well with the results of our previous study [29]. The PMA field tends to saturation at a Pd underlayer thickness of 2 nm.

We used a Co volume magnetization value of 1.42×10^6 A/m for the calculation of the energy of PMA for all samples. Magnetically polarized Pd layers adjacent to Co layers with a net effective thickness of 0.2 nm were neglected as layers with the magnetization 4.6 times lower than the magnetization in Co, $M_{s,Pd} \approx 3.1 \times 10^5$ A/m [31]. In the previous paper, we showed that a magnetic dead layer is formed at the interface of Co and Cu with the effective thickness of nearly 0.1 nm [29]. We considered this fact in the calculations of the Pd/Co/Cu and Cu/Co/Pd samples.

C. Velocity curves $v(H_x)$ of the DWs

The velocities of the left $\downarrow\uparrow$ and right $\uparrow\downarrow$ DWs driven by a constant positive OOP magnetic field were measured as functions of the IP magnetic field. The directions of the magnetic fields are outlined in Fig. 3(a). The shape of the $v(H_x)$ curves did not change when the magnitude of the OOP magnetic field was varied. All $v(H_x)$ curves of the selected sample merged when normalized to the value of the velocity at a minimum (see the Supplemental Material [25]). The velocity curves of the Cu/Co/Pd sample are reasonably symmetrical with the minima in the $|H_x| = 10$ mT [Fig. 3(b)]. The multiple nucleation of domains prevented us from measuring large velocities of the DWs in this sample. The shape of $v(H_x)$ curves in the Pd(0.22) sample become asymmetric because of the appearance of a kink in zero IP magnetic fields [Fig. 3(c)]. The position of the minimum only slightly shifts toward larger magnetic fields $|H_x| = 15$ mT. However, 0.4 nm of Pd on the bottom of the Co layer is sufficient to change the shape of $v(H_x)$ curves significantly. The $v(H_x)$ curves have two pronounced kinks: the first kink is observed in zero IP magnetic fields, and the second kink, which simultaneously

is a minimum, is in $|H_x| = 50$ mT [Fig. 3(d)]. The $v(H_x)$ curves became strongly asymmetrical. With an increase in the thickness of the bottom Pd layer, the following tendency is observed. The first kink of the $v_{\downarrow\uparrow}(H_x)$ curves shifts toward negative IP magnetic fields and becomes smoother. The minimum shifts toward positive IP magnetic fields [Figs. 3(e)–3(h)]. The difference between the values of the velocities at the first and second kinks increases with an increase in the Pd underlayer thickness. The general features of the $v(H_x)$ curves, which are observed in the Pd/Co/Pd trilayers with large Pd underlayer thickness, are present in the Pd(3)/Co/Cu sample [Fig. 3(i)]. The $v(H_x)$ curves of the Pd(3)/Co/Cu sample demonstrate kinks and are strongly asymmetrical.

The velocity curves of the samples were fitted by the extended dispersive stiffness model. The fitting parameters were the DMI field H_{DMI}, the DW anisotropy field H_B, the correlation length ξ, the chiral damping weight χ^*, and the velocity v_0^*. A fitting program searched for the minimal residual dispersion by means of variation of the fitting parameters. The fitted $v(H_x)$ curves are shown in Fig. 3 by solid lines.

D. DMI and chiral damping

The dependence of the effective DMI energy D_{eff} on the Pd bottom layer thickness is shown in Fig. 4(a). The DMI energy is defined as $D_{eff} = \mu_0 M_s \lambda H_{DMI}$, where $\lambda = \sqrt{A/K_{eff}}$ is a Bloch DW thickness and $A = 25$ pJ/m is the exchange constant for Co [19]. The shape of the $D_{eff}(d_{Pd})$ and $H_{DMI}(d_{Pd})$ dependencies is generally similar; however, the $\lambda(d_{Pd})$ function makes differences in the behavior of these two quantities. The negative effective DMI energy increases in the magnitude in the Pd bottom layer thickness interval from 0 to 0.2 nm. With further increase of the Pd bottom layer thickness, the magnitude of the effective DMI energy decreases. Here, D_{eff} changes the sign between the thicknesses of $d_{Pd} = 0.6$ and 1 nm and increases in the positive range up to 0.19 ± 0.05 mJ/m^2 with $d_{Pd} = 3$ nm, when the system becomes symmetric by the composition. Note that the asymmetric Pd(3)/Co/Cu sample has approximately zero DMI.

With a change in the Pd underlayer thickness from 0 to 0.4 nm, the absolute value of the chiral damping weight increases abruptly from 0.2 to 0.9 and oscillates near this value with
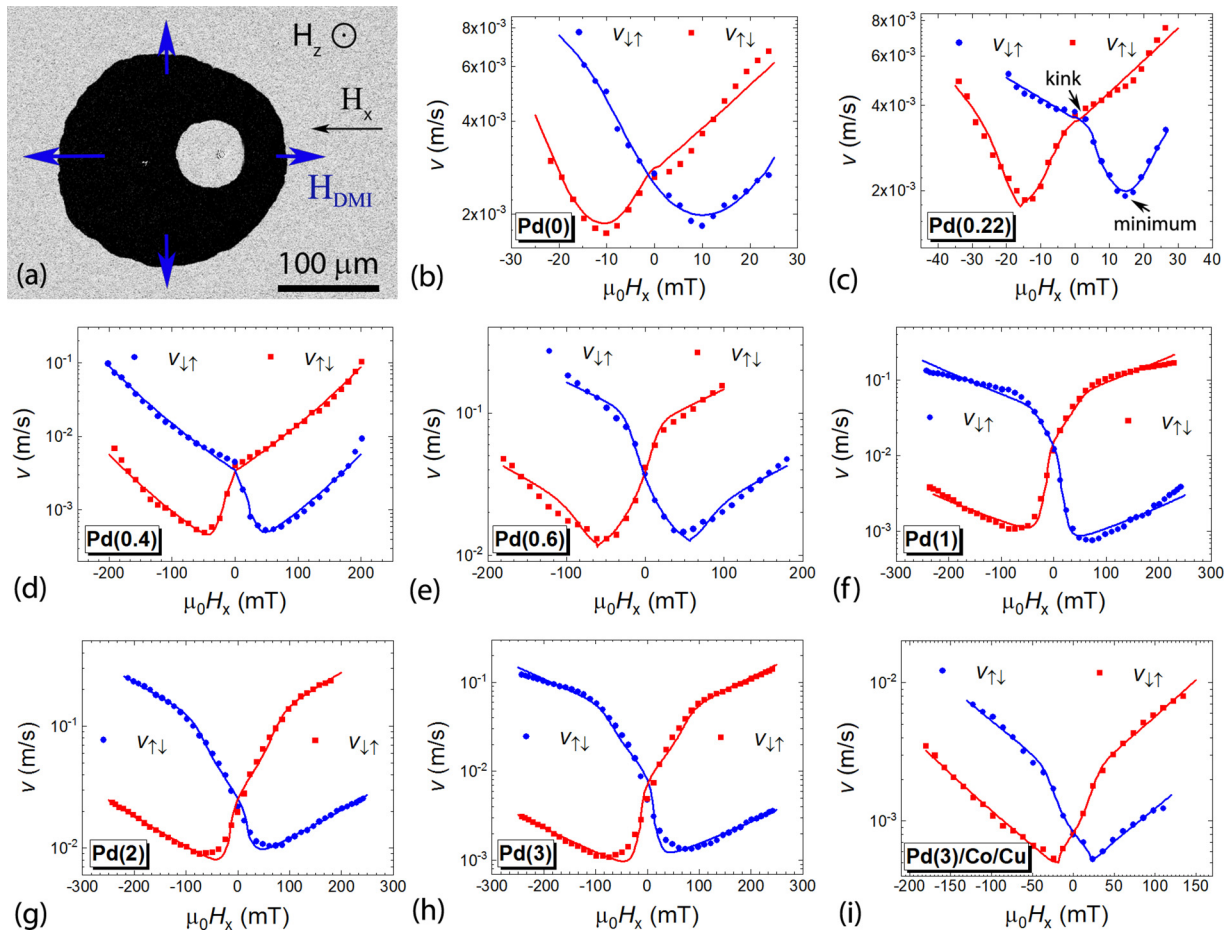
FIG. 3. (a) Scheme of the measurements. $v(H_x)$ curves measured in (b) Cu/Co/Pd, (c) Pd(0.22), (d) Pd(0.4), (e) Pd (0.6), (f) Pd(1), (g) Pd(2), (h) Pd(3), and (i) Pd(3)/Co/Cu samples. Squares and circles denote experimental points. Solid lines are calculated by the extended dispersive stiffness model.

a further increase of the bottom Pd thickness [Fig. 4(b)]. Strictly speaking, the physical nature of the asymmetry of $v(H_x)$ curves is under debate. In some studies, this effect is named chirality-induced [15,18] or additional asymmetry [9]. Elastic strains in the Co layers might play a significant role in the chirality-induced asymmetry of the $v(H_x)$ curves. This assumption is confirmed by an increase of the chiral damping weight if changing a stacking order in the asymmet-

ric samples from the Cu/Co/Pd to Pd/Co/Cu. In the second case, the sample is much more strained than in the first case. However, the behavior of the thickness dependencies of the chiral damping weight and elastic strains [Fig. 1(d)] is quite different.

The sign of the chiral damping weight does not change when the order of the layers changes in the asymmetrical system, like in the study of Lau *et al.* [17]. These experimental
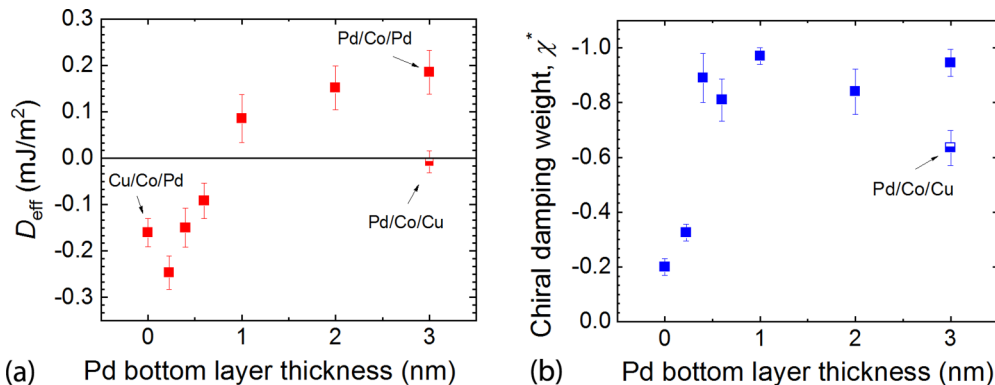

FIG. 4. Pd bottom layer thickness dependencies of (a) the effective Dzyaloshinskii-Moriya interaction (DMI) energy, (b) chiral damping weight. Half-shaded symbols denote data points for the Pd(3)/Co(0.7)/Cu(2) sample.

TABLE I. Strains in the interfaces and effective DMI energies for symmetric and asymmetric samples.

| Sample | Strains, $\eta = (a - a_{Co0})/a_{Co0}$ in | | D_{eff} (mJ/m^2) |
	Bottom interface (%)	Top interface (%)	
Pd(3)/Co(0.7)/Pd	9.4	4.3	0.19 ± 0.05
Pd(3)/Co(0.7)/Cu	9.4	4.3	-0.01 ± 0.02
Cu(2)/Co(0.7)/Pd	1.7	0.9	-0.16 ± 0.03

findings may suggest the possible volume origin of the considered effect. However, at the same time, the chiral weight is sensitive to the material deposited on the top of the Co layer. The chiral weight is 1.5 times more in the Pd(3)/Co/Pd sample than in the Pd(3)/Co/Cu one in spite of similar strain distributions in the samples. Further investigation of this system with variable thickness of the Co layers is needed to investigate the chiral damping effect more thoroughly.

The origin of the nonzero DMI in the symmetric Pd(3)/Co(0.7)/Pd(3) sample and the absence of the DMI in the asymmetric Pd(3)/Co/Cu sample may be related to a difference in the strains in the bottom Pd/Co and top Co/Pd interfaces. Comparing the Pd(3)/Co/Cu and Pd(3)/Co/Pd samples (see Table I) and considering that the DMI in the interface of Co with Cu is nearly zero because Cu is metal with a weak spin-orbit coupling, we may conclude that the top Co/Pd interface is mainly responsible for the existence of DMI in the symmetric Pd(3)/Co(0.7)/Pd(3) sample. The effective DMI energies for the both Cu/Co/Pd or Pd(0) and Pd(3)/Co/Pd samples are primarily defined by the contributions from the top interfaces. The contributions to the effective DMI energies from the bottom interfaces are nearly zero for both samples. However, the top Co/Pd interface is differently strained in these samples. Therefore, it may be assumed that the increase in the DMI in the Pd/Co/Pd samples with increasing Pd underlayer thickness is due to the increase in the strains in the top Co/Pd interface.

The assumption is based on the analysis of only edge points of the $D_{eff}(d_{Pd})$ dependence. It is better to consider the DMI energy for the entire set of samples for an analysis. Consider elastic strains as $\eta = [a(d_{Pd}) - a_{Co0}]/a_{Co0}$.

Then, the effective DMI energy in the Pd/Co/Pd trilayer is calculated as $D_{eff}(d_{Pd}) = D_{Pd/Co}(\eta) + D_{Co/Pd}(\eta)$. In general, knowledge of the only net DMI in the Pd/Co/Pd system does not allow us to calculate separate contributions to the effective DMI energy from the bottom Pd/Co and top Co/Pd interfaces. If we neglect the contribution to the DMI from the Cu/Co and Co/Cu interfaces, it becomes possible to evaluate $D_{Pd/Co}(9.4\%) = -0.01 \pm 0.02$ mJ/m^2, $D_{Co/Pd}(4.3\%) = 0.18 \pm 0.05$ mJ/m^2, and $D_{Co/Pd}(0.9\%) = -0.16 \pm 0.03$ mJ/m^2 just from the analysis of the data obtained from asymmetric Pd/Co/Cu, Cu/Co/Pd, and symmetric Pd(3)/Co(0.7)/Pd(3) samples. These points are basic for a calculation of DMI contributions from the bottom and top interfaces under different assumptions.

Knowing the $D_{Co/Pd}$ values at the limiting values of the elastic strains, one could assume the form of the $D_{Co/Pd}(\eta)$ dependence. Then the effective contribution to DMI from the bottom Pd/Co interface $D_{Pd/Co}(\eta)$ may be calculated. Suppose a parabolic $D_{Co/Pd}(\eta)$ dependency. Then the $D_{Pd/Co}(\eta)$ function takes a parabolic form as well [Fig. 5(a)]. One could see that the values of $D_{Pd/Co}$ and $D_{Co/Pd}$ taken at similar strains are nearly equal in magnitude but have opposite sign, which is expected due to a symmetry reason. Therefore, the complex behavior of the net DMI in the Cu/Pd/Co/Pd series of samples as the function of the Pd bottom layer thickness may be explained by universal parabolic dependencies of the contributions from the bottom and top interfaces to the net DMI on the strains $D_{Pd/Co}(\eta) \approx -D_{Co/Pd}(\eta)$.

A linear (or some other) $D_{Co/Pd}(\eta)$ dependence may be assumed [Fig. 5(b)], but it does not significantly change the result. In this case, the magnitudes of the interface contributions to the DMI are not equal at same strains, while general behavior of the dependencies is conserved. It is quite expectable since the interfaces may be structurally different, especially if they are not completely formed. The first three points of the $D_{Pd/Co}(\eta)$ dependencies are obtained in the samples with the effective thickness of the Pd bottom layer of 0.4 nm and less. Based on our previous study [30], we suppose that pure Pd begins to grow from the thickness of about 0.6 nm. We do not exclude intermixing of Pd with Cu in the initial stages of growth. Nevertheless, we may conclude that, firstly, the elastic strains in the interfaces strongly influence the magnitude and even the sign of the contributions to the net DMI energy from
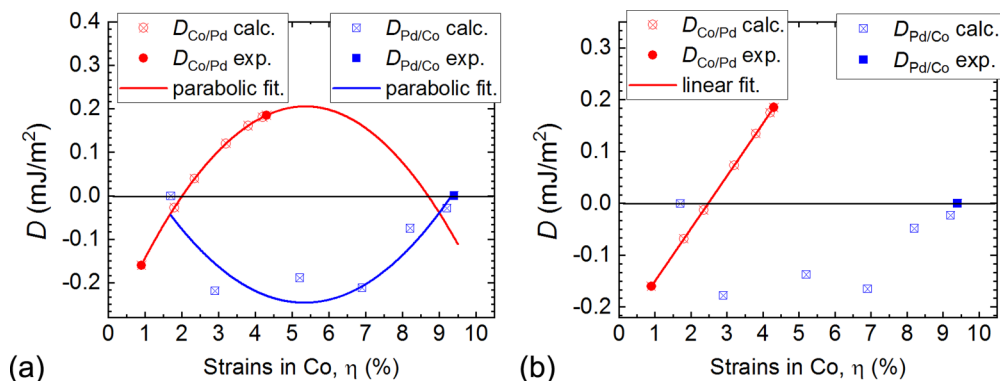

FIG. 5. The dependencies of $D_{Pd/Co}$ and $D_{Co/Pd}$ on elastic strains calculated under assumption of the (a) parabolic and (b) linear form of the $D_{Co/Pd}(\eta)$ function.
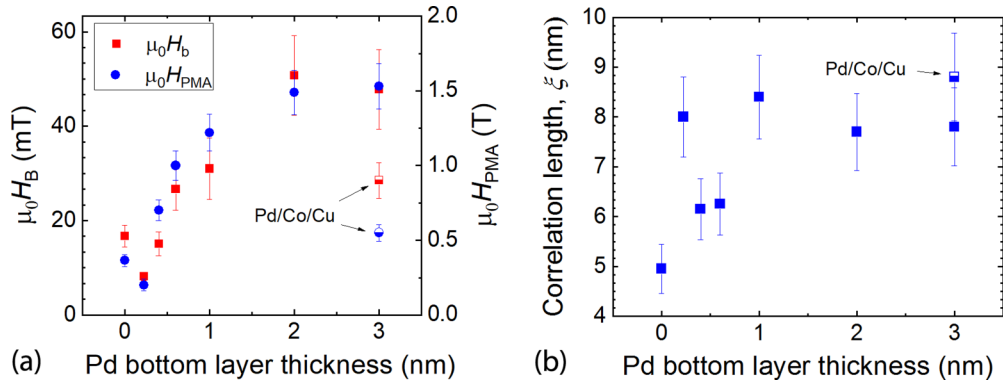
FIG. 6. Pd bottom layer thickness dependencies of (a) domain wall (DW) anisotropy and perpendicular magnetic anisotropy (PMA) fields, (b) correlation length in the Cu(2)/Pd(0–3)/Co(0.7)/Pd(3) samples. Half-shaded symbols denote data points for the Pd(3)/Co(0.7)/Cu(2) sample.

each interface. Secondly, the energy of the net effective DMI is defined by both contributions from the bottom and top interfaces which do not compensate each other in any of the considered samples because the interfaces are differently strained.

The DW anisotropy field H_b is the IP magnetic field oriented along a normal of a Bloch DW, which is needed to be applied to orient the magnetization inside the Bloch DW perpendicular to its plane. The dependence of the DW anisotropy field on the Pd underlayer thickness is shown in Fig. 6(a), and it correlates with the Pd thickness dependence of the effective magnetic anisotropy. The qualitative behavior of the $H_b(d_{Pd})$ dependence is straightforward. An increase in PMA leads to an increase in the demagnetizing factor of the Bloch DW and, consequently, its anisotropy field.

The final considered parameter is the correlation length. Based on our previous investigation, we expect an increase in the root-mean-square (RMS) roughness from 0.1 to 0.2 nm when the Pd underlayer with the thickness of 0.4 nm is deposited on the Si/Cu(2) surface [30]. Then the RMS roughness of Si/Cu(2)/Pd(d_{Pd}) does not change significantly up to the Pd thickness of 0.29 nm. The RMS roughness of the Co layers with the thickness of 0.7 nm deposited on the Pd underlayers is nearly the same as the RMS roughness of the Pd underlayers [29]. The Pd underlayer thickness dependence of the correlation length resembles the Pd thickness dependence of the RMS roughness, except the point at $d_{Pd} = 0.2$ nm. This may

be explained by correlation between the RMS roughness and the size of the islands, which corresponds to the magnitude of the correlation length reasonably well (see the Supplemental Material [25]).

E. Comparison of the results with literature data

If the chirality-induced asymmetry is zero, then the shape of the $v(H_x)$ curves is defined by the dependence of the DW energy density per unit area on the IP magnetic field, which is included in an exponential part of the creep law. For definiteness, consider the velocity of the left DW $v_{\downarrow\uparrow}$. An exponential part of the $v(H_x)$ curve $\exp(-\Delta E/k_B T)$ or v/v_0 normalized to the minimal value calculated by the extended dispersive-stiffness model for the Pd(3) sample is shown in Fig. 7(a). The shape of the normalized v/v_0 curve is characterized by a gradual decrease, when the IP magnetic field is changed from zero to the H_{min} value, and a rapid increase, when the IP magnetic field is less than the H_{min} value. It is noteworthy that the kinks in the normalized v/v_0 curves may be rather smooth in this case and may be difficult to observe in the experimental $v(H_x)$ curves. The absolute value of the $-H_{DMI}$ field is slightly larger than the $|H_{min}|$ value in this case. Hence, the absolute value of the DMI field defined by the position of the minimum in the $v(H_x)$ curve will be underestimated in this
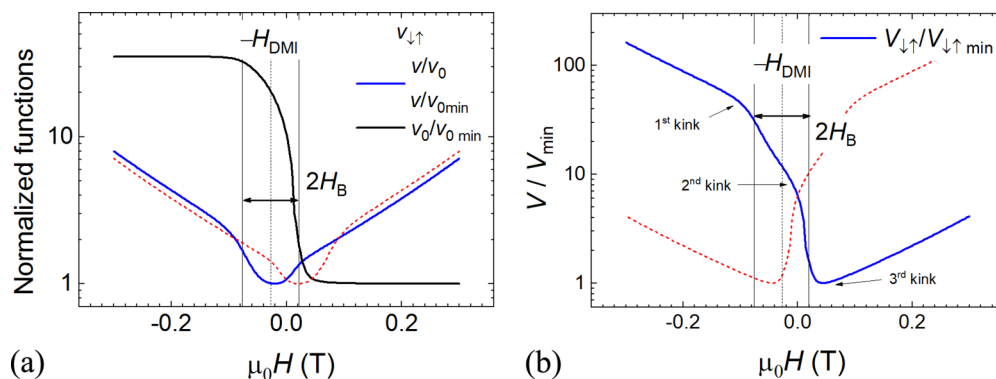

FIG. 7. In-plane (IP) magnetic field dependencies of (a) $\ln(v/v_0)$ and v_0 and (b) the resulting velocity v calculated with the chiral damping weight, $\chi^* = -0.95$ for the Pd(3) sample. All functions are normalized to their minimal values for scaling. Red dashed lines denote data calculated for the $v_{\uparrow\downarrow}(H_x)$ curves.
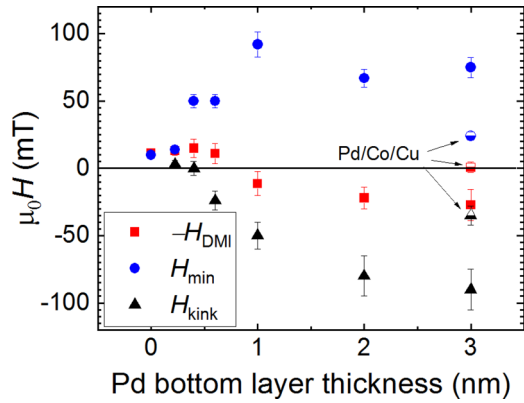
FIG. 8. Pd bottom layer thickness dependencies of $-H_{DMI}$ and in-plane (IP) magnetic fields, at which the minimum and the first kink are observed in the $v_{\downarrow\uparrow}(H_x)$ curves.

case. This finding was experimentally confirmed in samples demonstrating the $v(H_x)$ curves of such a shape [15,23].

The normalized $v_0(H_x)$ dependence calculated for the Pd(3) sample is shown in Fig. 7(a) for comparison with the exponential part. The velocity prefactor changes in the IP magnetic field interval where DWs have an intermediate Bloch-Néel structure [16]. Note that the velocity prefactor saturates if $|H_x - H_{DMI}| \gg H_B$. The reason for an incomplete saturation of the velocity prefactor in the area of $|H_x - H_{DMI}| = H_B$ is related to the constant value of $\alpha = 8°$ used for the calculation of the exponential part [21,22]. The normalized $v_0(H_x)$ dependence is asymmetric relative to the DMI field in the IP magnetic field interval $|H_x - H_{DMI}| < H_B$ for the same reason. See the Supplemental Material [25], in which the $v_0(H_x)$ dependence calculated with the optimized α is considered.

Product of the two aforementioned factors gives the resulting $v(H_x)$ curve shown in Fig. 7(b). The shape of the curve is characterized by a rapid decrease in the velocity with an increase in the IP magnetic field to the H_{min} value and a subsequent gradual increase of the velocity in larger IP magnetic fields. The velocities equidistant from the $-H_{DMI}$ field are not equal in any nonzero IP magnetic fields. The $v(H_x)$ curves demonstrate three kinks. The first kink is related to the beginning of a transformation of the magnetic structure of the DWs from the Néel to Bloch type. In this case, both the exponent and the velocity prefactor decrease. The second kink is defined by a strong decrease in the velocity prefactor, which even overcomes an increase in the exponent. The third kink and simultaneously the minimum is caused by a saturation of the magnetic structure of the DW to the Néel type and, hence, an increase in the exponential factor while the velocity prefactor becomes constant. Evidently, the $-H_{DMI}$ field must be in the magnetic field region between the first and third kinks, in which the transformation of the magnetic structure of the DW occurs. Indeed, the $-H_{DMI}$ field does not coincide with the magnetic field $\mu_0 H_{min}$, at which the minimum in the $v(H_x)$ curves is observed, except for two beginning points of the Pd(0) and Pd(0.2) samples, in which the chiral damping weight is minimal (Fig. 8).

In the case of large chiral damping, the shape of the $v(H_x)$ curves is mainly defined by the IP magnetic field depen-

dence of the velocity prefactor. Experimental $v(H_x)$ curves are strongly asymmetric. Since the asymmetry of the $v(H_x)$ curves caused by their dispersive stiffness and chiral damping is multiplied, the relative difference between the minimum and maximum velocities in Fig. 7(b) reaches two orders of magnitude. Such strongly asymmetric $v(H_x)$ curves are frequently observed in experimental studies of the DWs dynamics [9,17,32]. It is noteworthy that the asymmetric $v(H_x)$ curves obtained in this paper could not be fitted only with the exponential part of the creep law without considering the chirality-dependent velocity prefactor.

The obtained results indicate that even rough estimation of the DMI field only from the position of the minima in the $v(H_x)$ curves may lead to wrong results. The $v(H_x)$ curves must be measured in a wide range of magnetic fields to analyze their overall shape. It is necessary to detect not only minima in the $v(H_x)$ curves but reach the saturation in the $v(H_x)$ dependencies. The kinks before the saturation indicate the complete transformation of DWs from Bloch to Néel type [15,22] and define the DW anisotropy field.

V. CONCLUSIONS

DW propagation in the creep regime was investigated in epitaxial Cu(2)/Pd(d_{Pd})/Co(0.7)/Pd(3) structures in simultaneously applied IP and OOP magnetic fields. The thickness of the bottom Pd layer was varied from 0 to 3 nm. The measured $v(H_x)$ curves were fitted by an extended dispersive-stiffness model. With increasing thickness of the Pd bottom layer >0.4 nm, the $v(H_x)$ curves became strongly asymmetric. Analysis of the fittings indicates that the asymmetry in the $v(H_x)$ curves is mainly caused by the dependence of the velocity prefactor in the creep law on the internal magnetic structure of the DWs, which may be related to the chiral damping effect. The absolute value of the chiral damping weight increased from 0.2 to 0.9 with an increase of the thickness of the Pd bottom layer. The Pd bottom layer thickness dependence of the effective DMI is complex. With a slight decrease of D_{eff} in the Pd thickness interval from 0 to 0.23 nm, the effective DMI energy increased from -0.25 ± 0.04 to 0.19 ± 0.05 mJ/m^2 with increasing Pd underlayer thickness from 0.23 to 3 nm. We related the increase of the effective DMI in the symmetric system to the dependencies of the contributions to the effective DMI from the bottom Pd/Co and top Co/Pd interfaces on elastic strains and asymmetry of the elastic strains in the bottom and top interfaces.

[1] A. Fert, V. Cros, and J. Sampaio, Nat. Nanotechnol. **8**, 152 (2013).

[2] S. Parkin and S. H. Yang, Nat. Nanotechnol. **10**, 195 (2015).

[3] W. J. Jiang, G. Chen, K. Liu, J. D. Zang, S. G. E. te Velthuis, and A. Hoffmann, Phys. Rep. **704**, 1 (2017).

[4] G. Chen, J. Zhu, A. Quesada, J. Li, A. T. N'Diaye, Y. Huo, T. P. Ma, Y. Chen, H. Y. Kwon, C. Won, Z. Q. Qiu, A. K. Schmid, and Y. Z. Wu, Phys. Rev. Lett. **110**, 177204 (2013).

[5] S. Emori, U. Bauer, S. M. Ahn, E. Martinez, and G. S. D. Beach, Nat. Mater. **12**, 611 (2013).

[6] T. H. Pham, J. Vogel, J. Sampaio, M. Vanatka, J.-C. Rojas-Sanchez, M. Bonfim, D. S. Chaves, F. Choueikani, P. Ohresser, E. Otero, A. Thiaville, and S. Pizzini, Epl-Europhys. Lett. **113**, 67001 (2016).

[7] Y. Yoshimura, K.-J. Kim, T. Taniguchi, T. Tono, K. Ueda, R. Hiramatsu, T. Moriyama, K. Yamada, Y. Nakatani, and T. Ono, Nat. Phys. **12**, 157 (2016).

[8] S. G. Je, D. H. Kim, S. C. Yoo, B. C. Min, K. J. Lee, and S. B. Choe, Phys. Rev. B **88**, 214401 (2013).

[9] D.-Y. Kim, N.-H. Kim, Y.-K. Park, M.-H. Park, J.-S. Kim, Y.-S. Nam, J. Jung, J. Cho, D.-H. Kim, J.-S. Kim, B.-C. Min, S.-B. Choe, and C.-Y. You, Phys. Rev. B **100**, 224419 (2019).

[10] C. Moreau-Luchaire, C. Moutafis, N. Reyren, J. Sampaio, C.A.F. Vaz, N. Van Horne, K. Bouzehouane, K. Garcia, C. Deranlot, P. Warnicke, P. Wohlhüter, J. M. George, M. Weigand, J. Raabe, V. Cros, and A. Fert, Nat. Nanotechnol. **11**, 444 (2016).

[11] A. W. J. Wells, P. M. Shepley, C. H. Marrows, and T. A. Moore, Phys. Rev. B **95**, 054428 (2017).

[12] J. W. Yu, X. P. Qiu, Y. Wu, J. Yoon, P. Deorani, J. M. Besbas, A. Manchon, and H. Yang, Sci. Rep. **6**, 32629 (2016).

[13] S. D. Pollard, J. A. Garlow, J. W. Yu, Z. Wang, Y. M. Zhu, and H. Yang, Nat. Commun. **8**, 14761 (2017).

[14] A. Hrabec, N. A. Porter, A. Wells, M. J. Benitez, G. Burnell, S. McVitie, D. McGrouther, T. A. Moore, and C. H. Marrows, Phys. Rev. B **90**, 020402(R) (2014).

[15] D.-Y. Kim, M.-H. Park, Y.-K. Park, J.-S. Kim, Y.-S. Nam, D.-H. Kim, S.-G. Je, H.-C. Choi, B.-C. Min, and S.-B. Choe, NPG Asia Mater. **10**, e464 (2018).

[16] E. Jué, C. K. Safeer, M. Drouard, A. Lopez, P. Balint, L. Buda-Prejbeanu, O. Boulle, S. Auffret, A. Schuhl, A. Manchon, I. M. Miron, and G. Gaudin, Nat. Mater. **15**, 272 (2016).

[17] D. Lau, J. P. Pellegren, H. T. Nembach, J. M. Shaw, and V. Sokalski, Phys. Rev. B **98**, 184410 (2018).

[18] D.-Y. Kim, M.-H. Park, Y.-K. Park, J.-S. Kim, Y.-S. Nam, H.-S. Hwang, D.-H. Kim, S.-G. Je, B.-C. Min, and S.-B. Choe, Phys. Rev. B **97**, 134407 (2018).

[19] A. V. Davydenko, A. G. Kozlov, A. G. Kolesnikov, M. E. Stebliy, G. S. Suslin, Y. E. Vekovshinin, A. V. Sadovnikov, and S. A. Nikitov, Phys. Rev. B **99**, 014433 (2019).

[20] V. Jeudy, A. Mougin, S. Bustingorry, W. Savero Torres, J. Gorchon, A. B. Kolton, A. Lemaitre, and J. P. Jamet, Phys. Rev. Lett. **117**, 057201 (2016).

[21] J. P. Pellegren, D. Lau, and V. Sokalski, Phys. Rev. Lett. **119**, 027203 (2017).

[22] D. M. F. Hartmann, R. A. Duine, M. J. Meijer, H. J. M. Swagten, and R. Lavrijsen, Phys. Rev. B **100**, 094417 (2019).

[23] K. Shahbazi, J. V. Kim, H. T. Nembach, J. M. Shaw, A. Bischof, M. D. Rossell, V. Jeudy, T. A. Moore, and C. H. Marrows, Phys. Rev. B **99**, 094409 (2019).

[24] J. Gorchon, S. Bustingorry, J. Ferre, V. Jeudy, A. B. Kolton, and T. Giamarchi, Phys. Rev. Lett. **113**, 027205 (2014).

[25] See Supplemental Material at http://link.aps.org/supplemental/10.1103/PhysRevB.103.094435 for detailed description of the extended dispersive stiffness model, which includes Refs. [26–28].

[26] S. Lemerle, J. Ferré, C. Chappert, V. Mathet, T. Giamarchi, and P. Le Doussal, Phys. Rev. Lett. **80**, 849 (1998).

[27] G. Blatter, M. V. Feigel'man, V. B. Geshkenbein, A. I. Larkin, and V. M. Vinokur, Rev. Mod. Phys. **66**, 1125 (1994).

[28] V. Jeudy, R. Díaz Pardo, W. Savero Torres, S. Bustingorry, and A. B. Kolton, Phys. Rev. B **98**, 054406 (2018).

[29] A. V. Davydenko, A. G. Kozlov, A. V. Ognev, M. E. Stebliy, A. S. Samardak, K. S. Ermakov, A. G. Kolesnikov, and L. A. Chebotkevich, Phys. Rev. B **95**, 064430 (2017).

[30] A. V. Davydenko, A. G. Kozlov, A. V. Ognev, M. E. Stebliy, and L. A. Chebotkevich, Appl. Surf. Sci. **384**, 406 (2016).

[31] H. Sakurai, F. Itoh, Y. Okabe, E. Oike, and H. Hashimoto, J. Magn. Magn. Mater. **198**, 662 (1999).

[32] R. Lavrijsen, D. M. F. Hartmann, A. van den Brink, Y. Yin, B. Barcones, R. A. Duine, M. A. Verheijen, H. J. M. Swagten, and B. Koopmans, Phys. Rev. B **91**, 104414 (2015).